

Journal of Biomedical Optics

SPIEDigitalLibrary.org/jbo

Numerical investigation of the effects of shear waves in transcranial photoacoustic tomography with a planar geometry

Robert W. Schoonover
Lihong V. Wang
Mark A. Anastasio



SPIE

Numerical investigation of the effects of shear waves in transcranial photoacoustic tomography with a planar geometry

Robert W. Schoonover, Lihong V. Wang, and Mark A. Anastasio

Washington University in St. Louis, Department of Biomedical Engineering, St. Louis, Missouri

Abstract. Using a recently developed reconstruction method for photoacoustic tomography (PAT) valid for a planar measurement geometry parallel to a layered medium, we investigate the effects of shear wave propagation in the solid layer upon the ability to estimate Fourier components of the object. We examine this ability as a function of the thickness of the layer supporting shear waves as well as of the incidence angle of the field in the planewave representation. Examples are used to demonstrate the importance of accounting for shear waves in transcranial PAT. Error measures are introduced to quantify the error found when omitting shear waves from the forward model in PAT. © 2012 Society of Photo-Optical Instrumentation Engineers (SPIE). [DOI: 10.1117/1.JBO.17.6.061215]

Keywords: attenuation; image reconstruction; photoacoustics; shear waves; tomography.

Paper 11651SS received Nov. 4, 2011; revised manuscript received Jan. 12, 2012; accepted for publication Feb. 8, 2012; published online May 10, 2012.

1 Introduction

Photoacoustic tomography (PAT) is a noninvasive biomedical imaging technique, based on the photoacoustic effect, which combines the optical absorption contrast of tissue with the high spatial resolution of ultrasound imaging techniques.¹⁻⁴ In PAT, the target is illuminated with a short optical pulse and an acoustic pressure signal is generated via the thermoacoustic effect.^{2,3} Wide-band ultrasonic transducers are used to measure the pressure signal at a number of locations outside the object and the measured data serve as the input to numerical image reconstruction algorithms that estimate the total absorbed optical energy density. The utility of PAT has been demonstrated in a number of *in vivo* studies of biological structure and function⁵⁻⁷ and in facilitating a number of medically relevant diagnostic tasks.^{2,8-13}

Functional imaging of mouse brains has been successfully demonstrated with PAT.^{5,6} For larger animals with thicker skulls, PAT has been demonstrated to provide qualitatively useful images of brain structures;¹⁴⁻¹⁷ however, the transmission of ultrasonic waves through the skull bone(s) induces strong changes to the photoacoustic signal through the processes of absorption, strong reflections, and longitudinal-to-shear mode conversion. These effects can result in distortions and degraded spatial resolution in the reconstructed images. Time-reversal algorithms for PAT have been shown to compensate for density variations, dispersion and absorption,¹⁸ but they do not account for media that support shear wave propagation.

Under the assumption that the to-be-imaged object is embedded in a planar, layered medium, the effects of absorption, dispersion, and shear-mode conversion can be compensated for using a recently derived PAT reconstruction formula.¹⁹ The reconstruction formula, which is based on the angular spectrum representation of the photoacoustic field, estimates the Fourier components of the absorbed optical energy density. In this

paper, the PAT reconstruction formula valid for planar, layered media is used to evaluate the role of modeling shear waves in PAT. Specifically, the transmission function for a three layer system when shear waves are modeled is compared to the transmission function for a three layer system for a system that does not compensate for shear waves. Comparisons are made based on the incident angle of the field in the plane wave representation as well as on the thickness of the solid layer. Object-independent error functions are introduced to quantify the importance of modeling shear waves for PAT in this geometry. We show that, when shear waves are omitted from the imaging model, a large number of Fourier components of the object will be mis-estimated.

2 Background

The assumed geometry of our system is shown in Fig. 1. The to-be-imaged object is contained in layer 2, characterized by speed of sound c_2 and density ρ_2 , where both are consistent with biological tissue (e.g., a fluid). The photoacoustic signal is detected in layer 0, on the plane $z = 0$, characterized by thickness d_0 , speed of sound c_0 , and density ρ_0 . Layer 1 is assumed to be a solid, thus supporting shear waves, with thickness d_1 . The solid is assumed to be dispersive and absorptive for both longitudinal and shear waves.

In PAT, the measured acoustic pressure is used to infer the absorbed optical energy density, denoted by $A(\mathbf{r})$. The space-frequency domain representation, $\tilde{p}(\mathbf{r}, \omega)$, of the acoustic field is related to the space-time representation, $p(\mathbf{r}, t)$, by a Fourier transform, viz

$$\tilde{p}(\mathbf{r}, \omega) = \int_{-\infty}^{\infty} dt p(\mathbf{r}, t) e^{i\omega t}, \quad (1)$$

where ω denotes the temporal frequency, $i \equiv \sqrt{-1}$, and $\mathbf{r} = (x, y, z)$. The pressure field away from the acoustic source can be expressed as

Address all correspondence to: Robert W. Schoonover and Mark A. Anastasio, Campus Box 1097, One Brookings Drive, St. Louis, Missouri 63130. Tel: 3125213030; E-mail: rschoono@seas.wustl.edu; anastasio@seas.wustl.edu

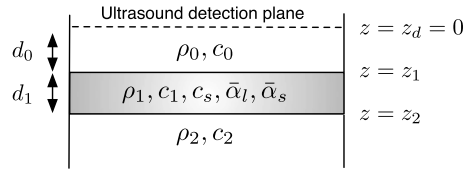


Fig. 1 A diagram of the layered system. Ultrasonic detection occurs in the plane $z = 0$. Layers 2 and 0 are assumed to be fluids, with densities ρ_m and speed of sound c_m . Layer 0 has thickness d_0 . Layer 1 is assumed to be a solid, bone, with density ρ_1 , longitudinal speed of sound c_l , shear speed of sound c_s , thickness d_1 , and longitudinal and shear absorption coefficients $\bar{\alpha}_l$ and $\bar{\alpha}_s$. The dispersive speeds of sound are referenced to 1 MHz. Layer 2 is assumed to be unbounded in the negative z -direction.

$$\bar{p}(\mathbf{r}, \omega) = i\omega\Gamma H(\omega) \iiint_V d^3r' G(\mathbf{r}, \mathbf{r}', \omega) A(\mathbf{r}'), \quad (2)$$

where $G(\mathbf{r}, \mathbf{r}', \omega)$ is an appropriate Green function that accounts for the detection system and appropriate boundary conditions, Γ is the Grueneisen parameter, $H(\omega)$ is the temporal Fourier transform of the exciting optical pulse's temporal profile, and $A(\mathbf{r})$ is the absorbed optical energy density. In Cartesian coordinates, $A(\mathbf{r}) \equiv A(x, y, z)$. The Green function has been previously expressed for planar detection in a homogeneous medium²⁰ and for planar detection in a layered medium.^{19,21}

Let $\bar{p}(k_x, k_y, \omega)$ denote the two-dimensional (2-D) spatial Fourier transform of the pressure data $\bar{p}(x, y, z, \omega)$ evaluated on the measurement plane $z = 0$:

$$\bar{p}(k_x, k_y, \omega) = \iint_{-\infty}^{\infty} dx dy \bar{p}(x, y, z = 0, \omega) e^{-i(k_x x + k_y y)}. \quad (3)$$

Similarly, let $\mathcal{A}(k_x, k_y, k_z)$ denote the three-dimensional Fourier transform of $A(x, y, z)$:

$$\mathcal{A}(k_x, k_y, k_z) = \iiint_{-\infty}^{\infty} dx dy dz A(x, y, z) e^{-i(k_x x + k_y y + k_z z)}. \quad (4)$$

It has been shown^{19,20} that certain Fourier components of the object can be estimated from the measured pressure via the relation

$$\mathcal{A}(k_x, k_y, k_z^{(2)}) = \frac{-2k_z^{(2)}}{\omega\Gamma H(\omega)T(\mathbf{k}_{\parallel}, \omega)} \frac{\rho_2 c_2}{\rho_0 c_0} e^{-ik_z^{(0)} d_0} \bar{p}(k_x, k_y, \omega), \quad (5)$$

where $\mathbf{k}_{\parallel} = (k_x, k_y, 0)^T$,

$$k_z^{(n)}(\mathbf{k}_{\parallel}, \omega) = \sqrt{\omega^2/c_n^2 - k_x^2 - k_y^2}, \quad (6)$$

d_0 is the distance between the detector and the last interface, and $T(\mathbf{k}_{\parallel}, \omega)$ is the planewave amplitude transmission function (ATF), which gives the relative amplitude and phase of the planewave that exits the layered system at $z = 0$ after insonification by a unit-amplitude monochromatic planewave at frequency ω , traveling in the direction parallel to $(k_x, k_y, k_z^{(2)})^T$ and incident on the layered medium from below. For measurement frequency ω_{\max} , the estimated values of \mathcal{A} lie inside a sphere in k -space of radius $k_{\text{rad}} = \omega_{\max}/c_2$, known as Ewald's sphere. The explicit form for T is derived in the Appendix for the three layer case. The function T captures the effects of dispersion, absorption, longitudinal-to-shear wave conversion, and the reflection and transmission of acoustic waves at the interfaces at $z = z_1$ and $z = z_2$. Note that for a homogeneous medium and object-to-detector distance, d , $T(\mathbf{k}_{\parallel}, \omega) = \exp(ik_z d)$ for all \mathbf{k}_{\parallel} and ω . For a planar, layered medium, the transmission function T is a function only of the magnitude of \mathbf{k}_{\parallel} . Without loss of generality, \mathbf{k}_{\parallel} is assumed to be of the form $(\omega \sin \theta/c_2, 0, 0)^T$

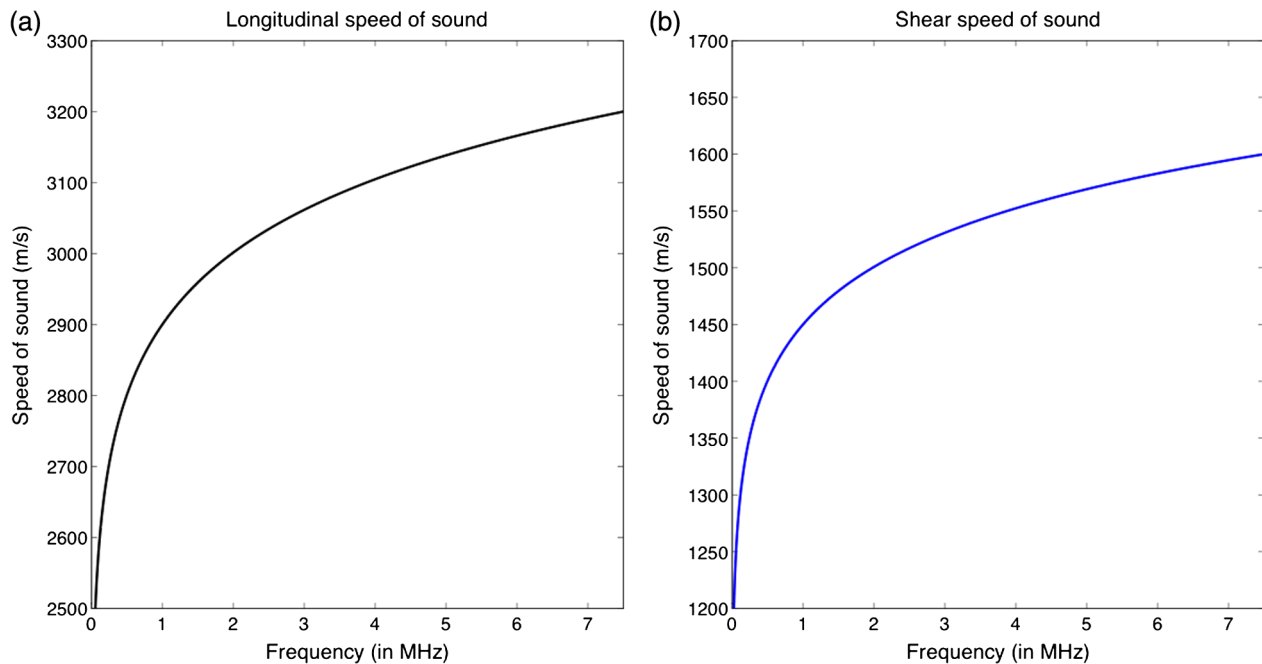


Fig. 2 (a) The longitudinal speed of sound as a function of frequency, (b) for the solid layer and the shear speed of sound. The medium is assumed to have known speeds of sound $c_l = 2900$ m/sec and $c_s = 1450$ m/sec at 1 MHz. The absorption coefficients are assumed to be $\bar{\alpha}_l = 81.13$ (Mrad/sec)^{-0.93} m⁻¹ and $\bar{\alpha}_s = 162.3$ (Mrad/sec)^{-0.93} m⁻¹. The speeds of sound averaged across the measurement band are $\bar{c}_l = 2785$ m/sec and $\bar{c}_s = 1392$ m/sec. At 1 MHz, $\alpha_l(\omega) = 170$ Np/m and $\alpha_s(\omega) = 341$ Np/m.

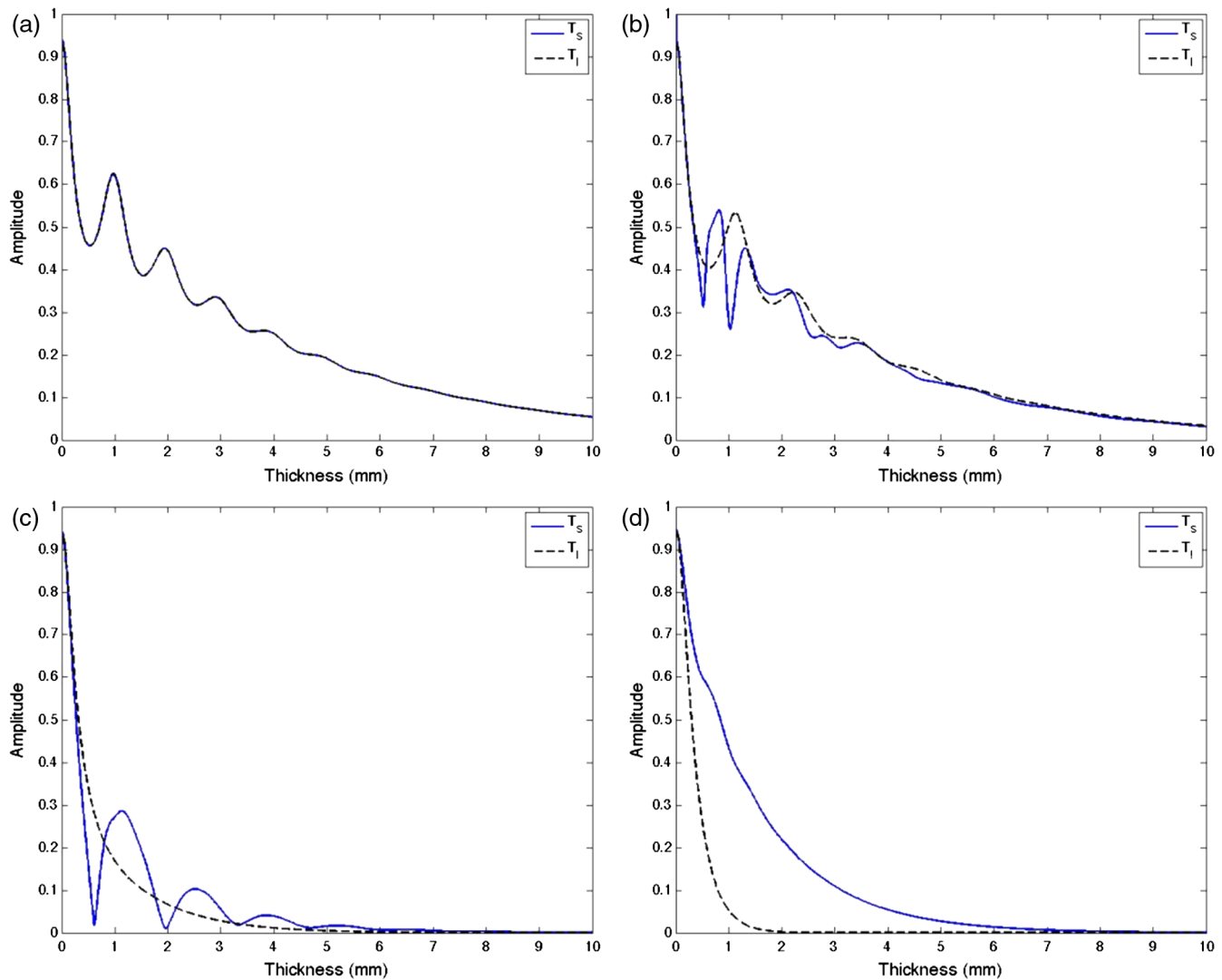


Fig. 3 The magnitude of the ATFs, $\bar{T}_l(\theta, \omega)$ (black dashes) and $\bar{T}_s(\theta, \omega)$ (blue line), as a function of the thickness of the solid layer for planewaves at $\omega = 2\pi \cdot 1.5$ MHz at an incidence angle of (a) 1 deg, (b) 15 deg, (c) 30 deg, and (d) 45 deg.

throughout this paper. That is, the wavevector is assumed to lie only in the $x - z$ plane, and is incident on the solid layer at an angle of θ .

Dispersion and absorption in the bone are both important effects that must be modeled to develop an accurate imaging model for transcranial PAT. For many tissues of interest, it is known²² that the linear absorption coefficient, as a function of temporal frequency, obeys a power law: $\alpha_m(\omega) = \bar{\alpha}_m |\omega|^y$. For $y \neq 1$, the dispersion relationship is given by²³

$$\frac{1}{c_m(\omega)} = \frac{1}{c_{0m}} + \alpha_m \tan\left(\frac{\pi y}{2}\right) (\omega^{y-1} - \omega_0^{y-1}), \quad (7)$$

where $c_m(\omega)$ is the speed of sound (longitudinal or shear) at frequency ω , c_{0m} is the known (measured) speed of sound at reference frequency ω_0 , and $m = 0, 1, 2, s$. Experimentally estimated values of the linear absorption coefficient for longitudinal waves in bone, $\alpha_l(\omega)$, range from 150 – 500 Np/m and the estimated values^{22,24–27} of y range from 0.8 to 1.3 at ultrasound frequencies. In Fig. 2, the longitudinal and shear speeds of sound are shown for $y = 0.93$ with the longitudinal

speed of sound at 1 MHz assumed to be 2900 m/sec, the shear speed of sound at 1 MHz assumed to be 1450 m/sec.

In this paper, we assumed a three-layer structure (see Fig. 1). The bottom layer was assumed to be soft tissue, unbounded in the $-z$ direction, with speed of sound 1483 m/sec and density 1000 kg/m³. The middle layer was assumed to be bone (a solid), with longitudinal speed of sound of 2900 m/s, shear speed 1450 m/sec at 1 MHz and density 1900 kg/m³. Both shear and longitudinal waves were assumed to obey a power law in the middle layer (bone) with $y = 0.93$ and $\alpha_l(\omega) = 170$ Np/m and $\alpha_s(\omega) = 341$ Np/m at 1 MHz. The choice of $y = 0.93$ falls within the reported ranges for power-law fitting.²⁶ The choices of α_l and α_s were chosen so that α_l fell within the range of reported absorption coefficients at 1 MHz and that the dispersive speeds of sound (shear and longitudinal) grew at similar rates. The top layer was assumed soft tissue, with speed of sound 1520 m/sec and density 1100 kg/m³. The thickness of the solid layer was varied in the simulations. The pressure wavefield was assumed to be recorded in a layer that is matched to the top layer a distance $d_0 = 1$ mm away from the tissue/bone edge.

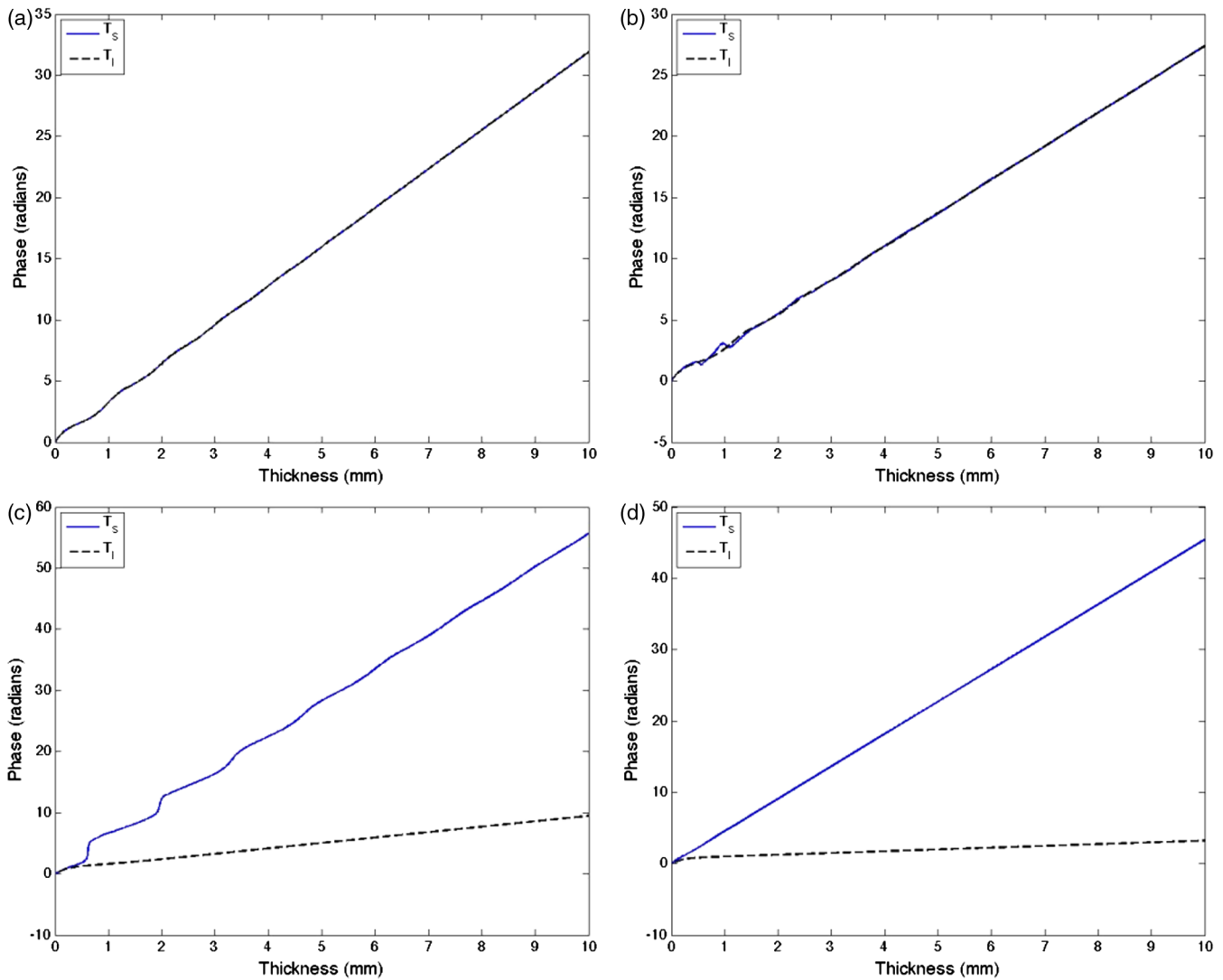


Fig. 4 The unwrapped phase of the ATFs, $\bar{T}_l(\theta, \omega)$ (black dashes) and $\bar{T}_s(\theta, \omega)$ (blue line), as a function of the thickness of the solid layer for plane waves at $\omega = 2\pi \cdot 1.5$ MHz at (a) an incidence angle of 1 deg, 15 deg, 30 deg, and (d) and 45 deg..

3 Transfer Function Analysis

The manner in which modeling shear waves in the PAT image reconstruction algorithm affects image quality in transcranial PAT is best understood by analyzing the ATF, $T(\mathbf{k}_{\parallel}, \omega)$, in Eq. (5). Let $\bar{T}_s(\theta, \omega) = T(\omega \sin(\theta)/c_2, \omega)$ denote the ATF for the layered medium when shear waves are modeled in layer 1. Let $\bar{T}_l(\theta, \omega) = T(\omega \sin(\theta)/c_2, \omega)$ denote the ATF for the layered medium when shear waves are not modeled in layer 1.

Plots of the magnitude and phase of \bar{T}_s and \bar{T}_l as a function of the thickness of the solid layer are shown in Figs. 3 and 4, with each panel representing a different incident plane wave angle. The assumed angular frequency is $\omega = 2\pi \cdot 1.5$ MHz. In Figs. 3(a) and 4(a), the incident plane wave angle is 1 deg. One notes that T_s and T_l are similar for all thicknesses. In the limit that the thickness goes to zero, the magnitude of the ATF tends toward 0.9401, the transmission coefficient for normal incidence for a two-layer medium with properties consistent with layer 0 and layer 2. In Fig. 4(b)–4(d), the ATFs are shown for an incident angle of 15, 30, and 45 deg, respectively. One sees that T_s and T_l differ greatly as the incidence angle increases for any thickness of the bone. For any incidence angle except zero degrees (normal incidence), the propagation of shear waves

will have some effect on the transmission of acoustic energy from layer 2 to layer 0, although that effect is best seen for larger angles. Moreover, one notes that \bar{T}_l at 30 and 45 deg falls off rapidly with thickness.

Plots of the magnitude and phase of \bar{T}_s and \bar{T}_l as a function of angle are shown in Figs. 5 and 6 for four different temporal frequencies. In panel a of each figure, the assumed angular frequency is $\omega = 2\pi \cdot 0.5$ MHz. In panel b, $\omega = 2\pi \cdot 1.0$ MHz, in panel c, $\omega = 2\pi \cdot 1.5$ MHz and in panel d, $\omega = 2\pi \cdot 2.0$ MHz. In all four panels, the thickness of the solid is assumed to be 2 mm. One notes that both the magnitude and phase of T_l and T_s are nearly identical for angles less than 25 deg in panels b, c, and d. Beyond that angle, the ATFs differ significantly. The critical angle for the fluid-solid interface found at 1 MHz is $\theta_c = \sin^{-1} \frac{1483}{2900} = 30.75$ deg, that is, acoustic plane waves incident on the interface at an angle greater than θ_c correspond to non-propagating longitudinal waves in the solid layer. Note that, due to the assumed dispersion relationship, the critical angle decreases with increased frequency from 1 MHz. Physically, for $\theta > \theta_c$, propagating shear waves generated at the fluid/solid interface between layers 2 and 1, traveling at 1450 m/sec at 1 MHz, transmit energy from one side of the solid to the

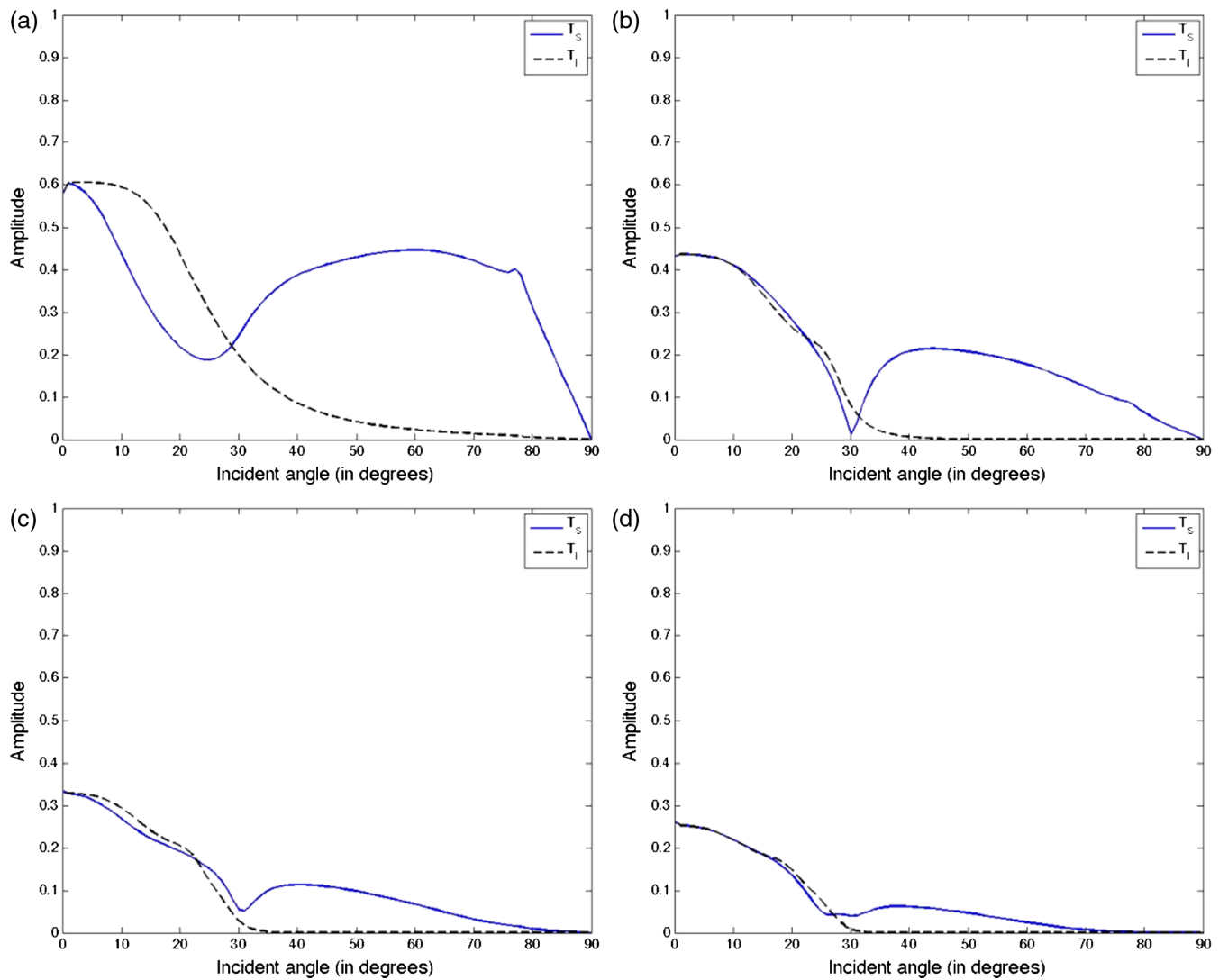


Fig. 5 The magnitude of the ATFs, $\bar{T}_l(\theta, \omega)$ (black dashes) and $\bar{T}_s(\theta, \omega)$ (blue lines), as a function of incident angle, for a bone layer with properties $d_1 = 3$ mm and (a) $\omega = 2\pi \cdot 0.5$ MHz, (b) $\omega = 2\pi \cdot 1.0$ MHz, (c) $\omega = 2\pi \cdot 1.5$ MHz, and (d) $\omega = 2\pi \cdot 2.0$ MHz.

other. The longitudinal waves are evanescent and decay rapidly from the interface between layers 2 and 1. When shear waves are not modeled, there is no mechanism for these high spatial frequency waves to transmit from one fluid medium (layer 2) to the other (layer 0). Accordingly, PAT reconstruction algorithms for planar layered medium that do not account for the propagation of shear waves will yield images with a inferior/lower lateral spatial resolution than algorithms that account for shear waves. These findings generalize beyond the choice of specific system parameters chosen in this paper. Varying the values of α_m and γ will only affect the rate at which the ATFs fall off as a function of thickness in Fig. 3, but the relationship between T_s and T_l will remain the same. Likewise, using different values for the speeds of sound or densities in the solid and fluid layers will change the critical angle, θ_c , but not the fact that T_s and T_l are in good agreement when the incident angle is less than the critical angle.

4 Error Analysis

It is clear that the ATF when shear waves are accounted for differs from the ATF when shear waves are not accounted for. These differences will manifest when attempting to

image objects through a solid layer in two ways. Since shear waves travel more slowly than longitudinal waves in the solid layer, misestimating the time-of-flight of the pressure field in the solid layer will lead to phase errors in the estimated Fourier components of the object. Likewise, errors in the estimated amplitude of the Fourier components of the object will occur because of not accounting for longitudinal-to-shear wave conversion and vice-versa at solid-fluid interfaces. Both effects will lead to distortions in the image.

To better understand the way in which not accounting for shear waves affects image fidelity, two error measures are introduced that are object-independent:

$$E_a(\mathbf{k}_{\parallel}, \omega) = \frac{|T_l(\mathbf{k}_{\parallel}, \omega)| - |T_s(\mathbf{k}_{\parallel}, \omega)|}{|T_s(\mathbf{k}_{\parallel}, \omega)|}, \quad (8)$$

$$E_p(\mathbf{k}_{\parallel}, \omega) = \angle T_s(\mathbf{k}_{\parallel}, \omega) - \angle T_l(\mathbf{k}_{\parallel}, \omega), \quad (9)$$

where \angle denotes the argument of a complex number. E_a denotes the estimated error in the amplitude of the Fourier component of the object and E_p denotes the estimated error in the phase of the Fourier component of the object. Note that E_a can be both

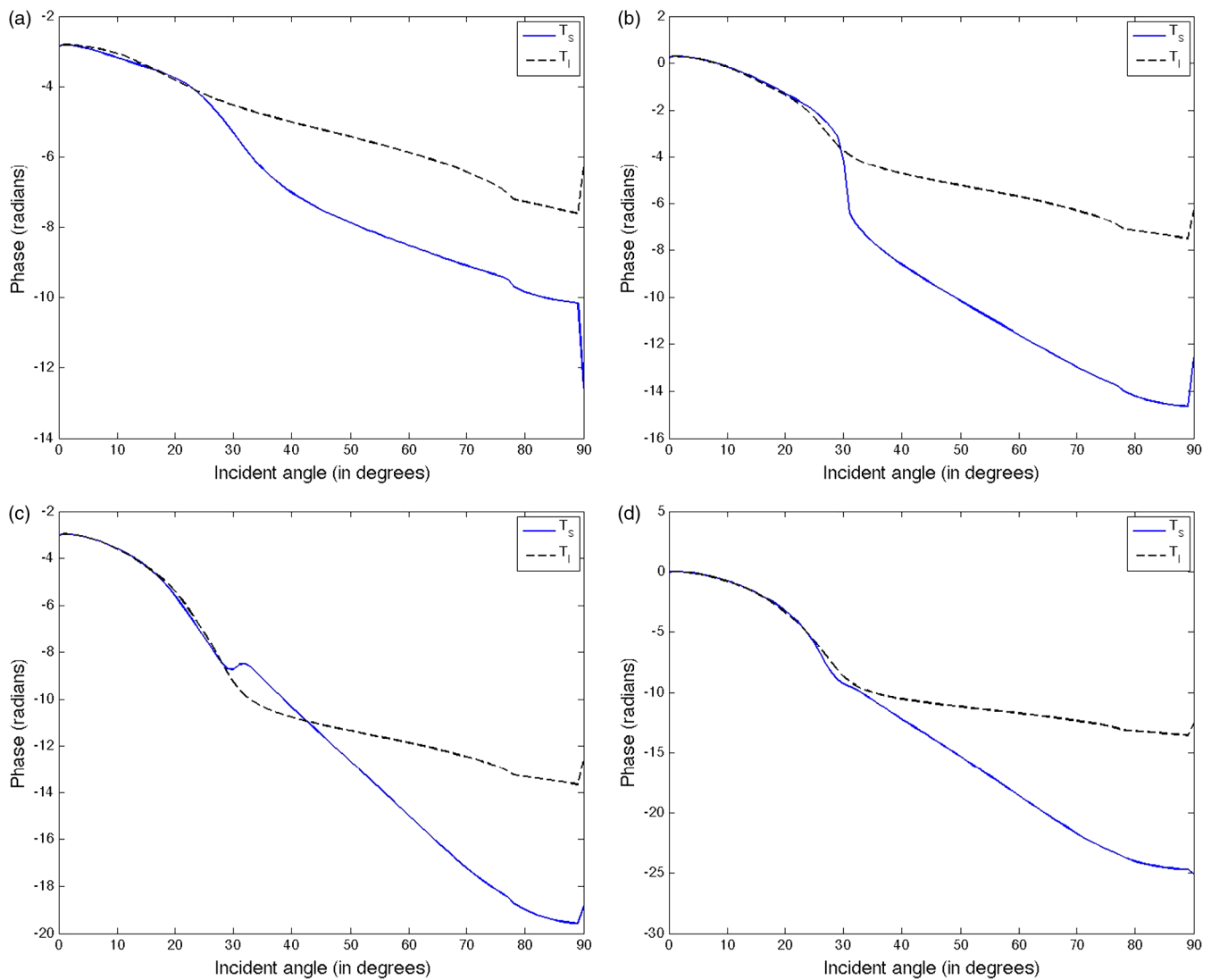


Fig. 6 The unwrapped phase of the ATFs, $\bar{T}_l(\theta, \omega)$ (black dashes) and $\bar{T}_s(\theta, \omega)$ (blue lines), as a function of incident angle, for a bone layer with properties $d_1 = 3$ mm and (a) $\omega = 2\pi \cdot 0.5$ MHz, (b) $\omega = 2\pi \cdot 1.0$ MHz, (c) $\omega = 2\pi \cdot 1.5$ MHz, and (d) $\omega = 2\pi \cdot 2.0$ MHz.

positive and negative. The positive error occurs when the model that omits shear waves overestimates the transmitted acoustic energy at a specific frequency and angle [see, for example, Fig. 5(a) from 10 to 25 deg]. The negative error occurs when the model that omits shear waves underestimates the transmitted acoustic energy, with a maximum negative error of -1 when the ATF for the model that omits shear waves is zero.

In Figs. 7–10, the amplitude and phase errors are shown in the $k_x - k_z$ plane for four different thicknesses of the solid layer. We assumed that the maximum measured frequency of the acoustic field in each case was 7.5 MHz, setting the radius of the Ewald measurement sphere at $k_{\max} = 2\pi \cdot 7.5 \text{ MHz} / c_2 = 31,776 \text{ m}^{-1}$. Note that E_a approaches -1 when T_l is near zero, i.e., the model that does not account for shear waves predicts a null value for the transmission amplitude.

In Fig. 7, the amplitude and phase error are shown when the solid layer is assumed to be $10 \mu\text{m}$ thick. One notes that the amplitude and phase error are relatively insignificant for small values of k_x for all k_z . However, larger errors exist for both the amplitude and phase near the line $k_z = 0$, with the size of the error growing for both amplitude and phase as k_x gets larger. In Fig. 8, the amplitude and phase error are

shown when the solid layer is assumed to be $100 \mu\text{m}$ thick. Even for this relatively thin layer, the amplitude distortions are already significant. The boundary between green and purple in the amplitude plot or between light blue and purple in the phase plot corresponds approximately to 28 deg, or near the critical angle, θ_c , for the fluid-solid interface. For larger incidence angles, the amplitude errors near -1 and the phase errors approach π .

In Fig. 9, the amplitude and phase error are shown when the solid layer is assumed to be 1 mm thick, and in Fig. 10, the amplitude and phase error are shown when the solid layer is assumed to be 1 cm thick. In both cases, which are relevant to primate brain imaging, one sees that the amplitude error is near -1 for all incidence angles above θ_c . This severely limits the ability of a non-shear wave based method for resolving large transverse frequency components of the to-be-imaged object in a planar detection geometry. In all figures, the maximum positive error in amplitude was set to be 3. The large positive error locations correspond to points at which T_s approaches 0 [see, for example, Fig. 5(b) at 30 deg].

To demonstrate the manner by which the errors in the ATFs due to neglecting shear waves can result in image artifacts,

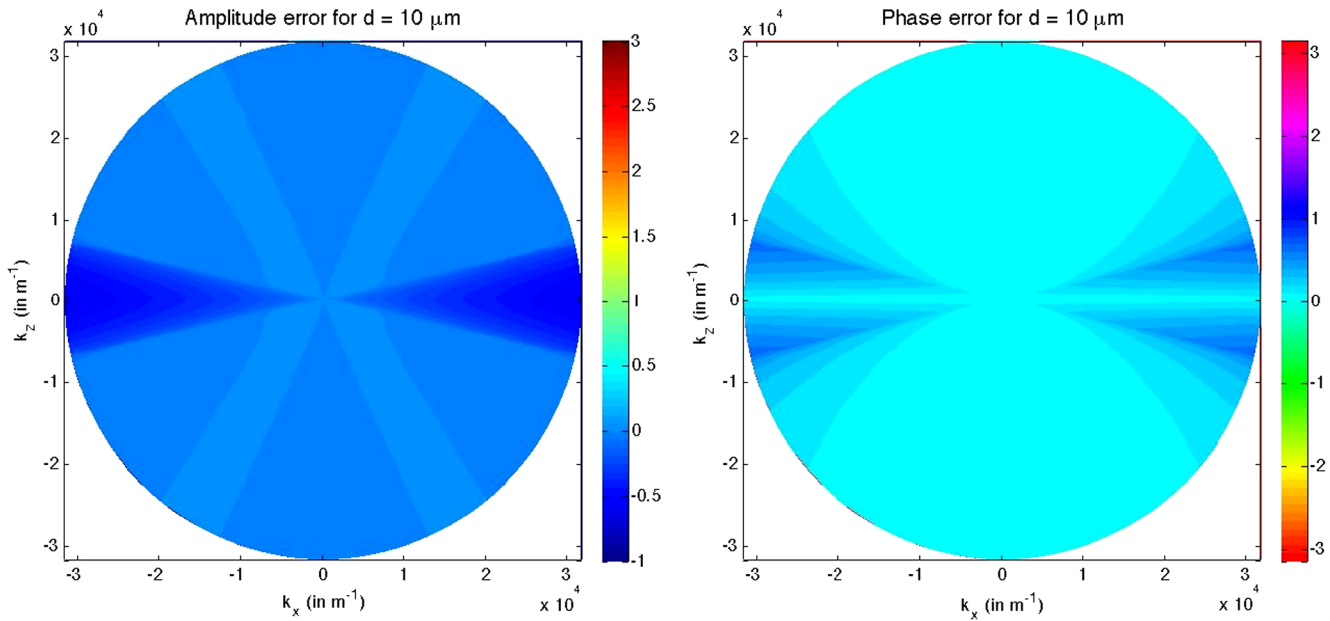


Fig. 7 The amplitude error, E_a , and the phase error, E_p , inside the Ewald measurement sphere, for a solid with thickness $d = 10 \mu\text{m}$.

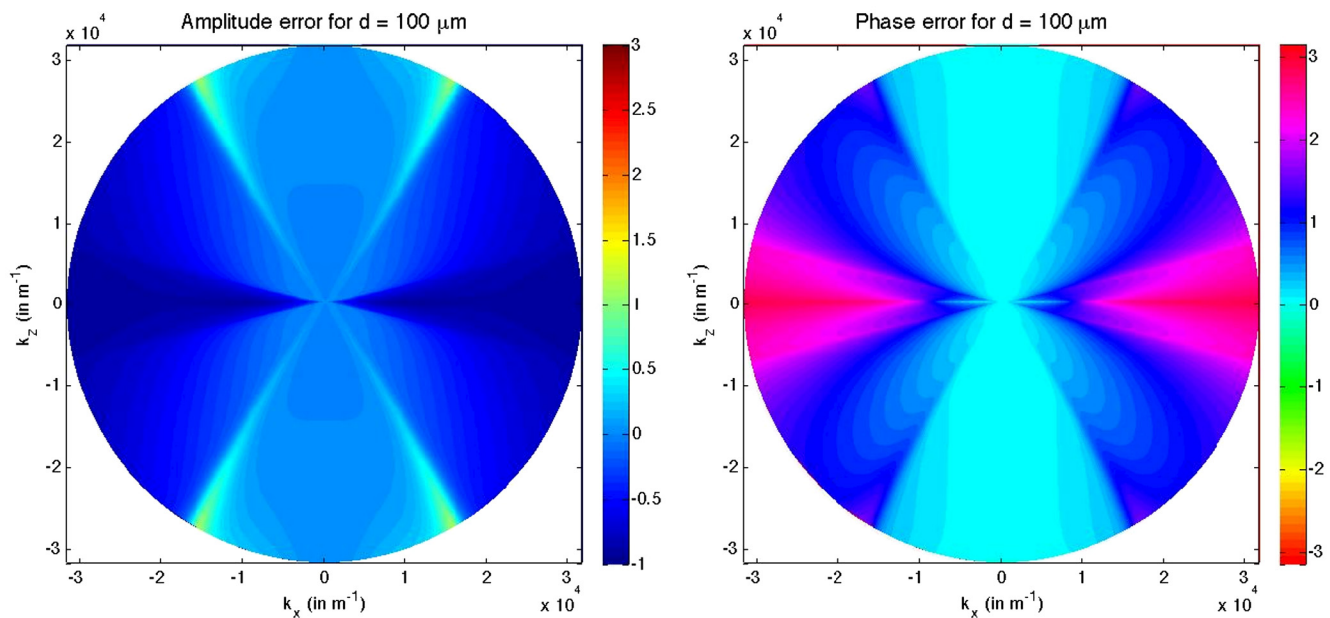


Fig. 8 The amplitude error, E_a , and the phase error, E_p , inside the Ewald measurement sphere, for a solid with thickness $d = 100 \mu\text{m}$.

computer-simulation studies were performed. Because the layered medium problem is inherently 2-D, only 2-D simulations were run. A numerical phantom representing the object, $A(\mathbf{r})$, was considered that consisted of three uniform disks of radii of 2, 3, and 4 mm, located within the bottom layer of the structure with centers along the line $x = 0$ [see Fig. 11(a)]. In these simulations, the solid layer was assumed to be the top edge of the image (i.e., the solid layer begins at the line $z = 25 \text{ mm}$). The disks were quasi-bandlimited by convolving each with a two-dimensional Gaussian function of radius $400 \mu\text{m}$. Uniform disks were employed in the simulations because their 2-D Fourier transforms are known analytically,

and therefore the simulated pressure data could be computed without numerical approximation. The object was assumed to be embedded in a the same three-layer structure as was described at the end of Sec. 2 (see Fig. 1) and was used in generating the error maps in Figs. 7–10.

Simulated pressure data were computed by use of $T_s(\mathbf{k}_{\parallel}, \omega)$, which properly modeled the effects of shear wave propagation in the solid layer. From these data, images were reconstructed by use of an inverse Fourier transform method that neglected shear wave propagation and employed the transfer function $T_l(\mathbf{k}_{\parallel}, \omega)$. A non-uniform sampling scheme in ω was assumed to avoid interpolation-based errors in the reconstructed images. This

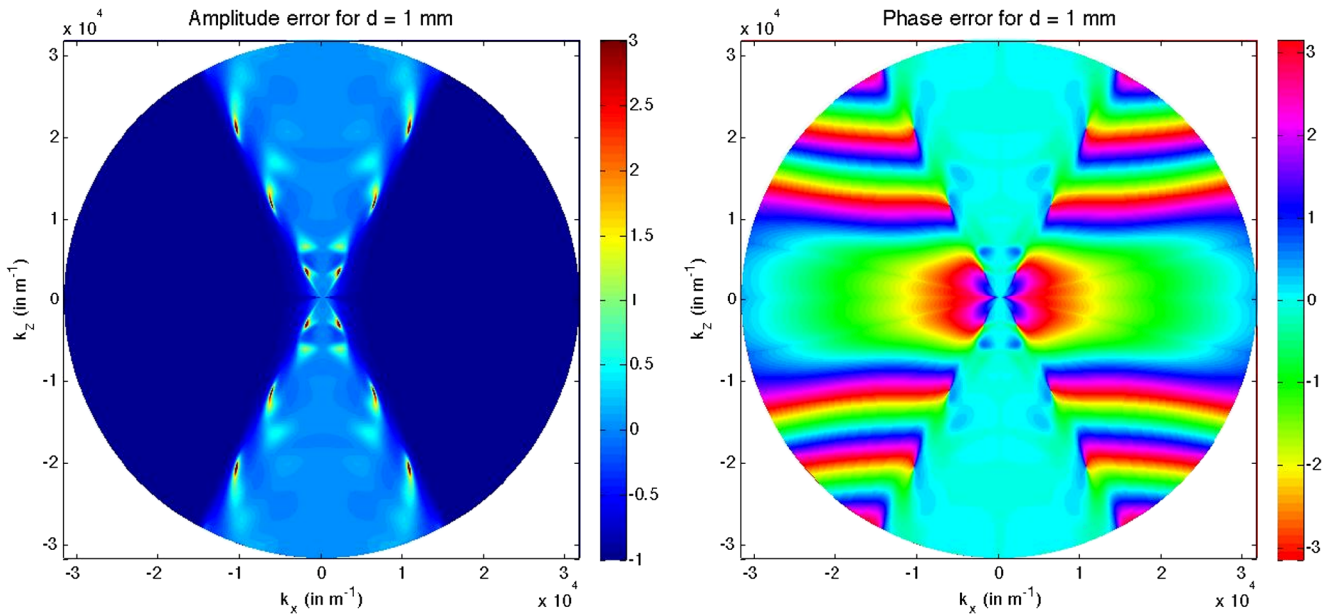


Fig. 9 The amplitude error, E_a , and the phase error, E_p , inside the Ewald measurement sphere, for a solid with thickness $d = 1$ mm. The maximum positive error in amplitude was set to be 3 to improve the dynamic range in the image.

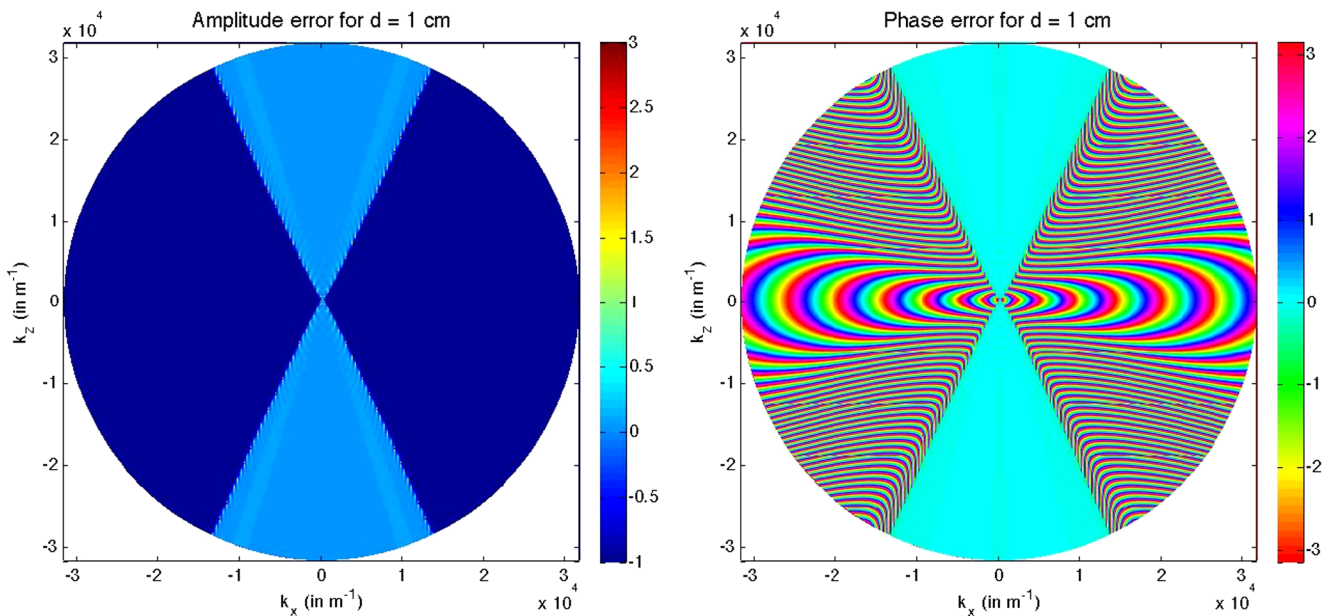


Fig. 10 The amplitude error, E_a , and the phase error, E_p , inside the Ewald measurement sphere, for a solid with thickness $d = 1$ cm. The maximum positive error in amplitude was set to be 3 to improve the dynamic range in the image.

prevented the confounding of model-mismatch errors (from neglecting shear waves), with errors associated with the specific reconstruction model used. For example, a Fourier-based inversion scheme, such as the one found in Ref. 19 requires interpolation of the data in the k_z -direction. Given that a known subset of Fourier components are misestimated when neglecting shear waves, inclusion of these data will result in an error that is unrelated to the errors associated with the neglect of shear waves. This assumption results in a reconstruction formula of the form

$$A_{ns}(x, z) = \frac{1}{(2\pi)^2} \iint dk_x dk_z \mathcal{A}(k_x, k_z) \times \frac{T_s[\mathbf{k}_{||}, \omega(k_x, k_z)]}{T_l[\mathbf{k}_{||}, \omega(k_x, k_z)]} e^{i(k_x x + k_z z)}, \quad (10)$$

where $A_{ns}(x, y)$ is the reconstructed object and $\omega(k_x, k_z) = \sqrt{k_x^2 + k_z^2}/c$ is the non-uniform sampling the temporal frequency domain. A discrete version of Eq. (10) was computed

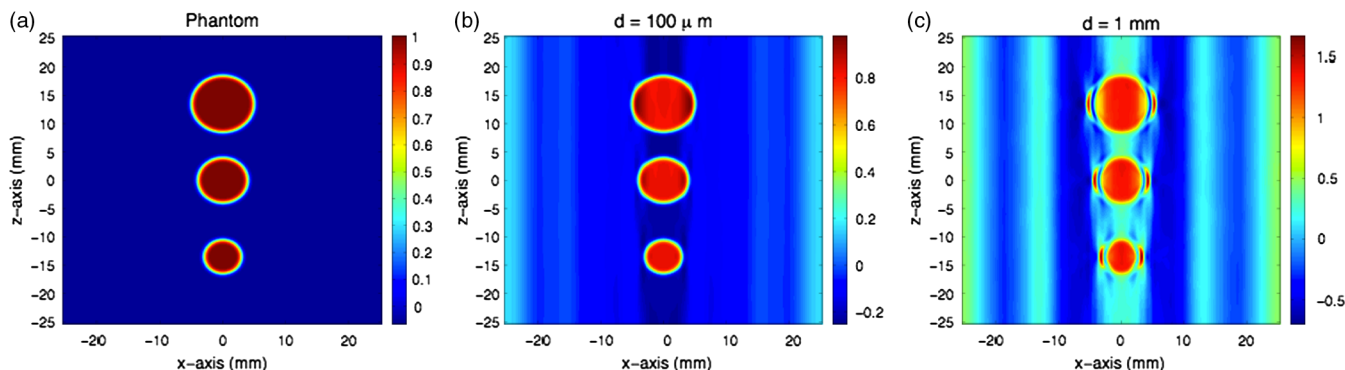


Fig. 11 (a) An image of the numerical phantom—three band-limited disks. (b) The reconstruction of those disks, found using Eq. (10), is shown when the solid layer is assumed to be $d = 100 \mu\text{m}$. (c) Reconstruction of those disks, found using Eq. (10), is shown when the solid layer is assumed to be $d = 1 \text{ mm}$.

as a 2-D discrete Fourier transform via the fast Fourier transform algorithm.

In Fig. 11(b), the reconstruction using Eq. (10) is shown for the case when T_s and T_l correspond to the solid (bone) layer being $100 \mu\text{m}$ thick. One notes that the reconstructed disks have slight errors, most prominent near the left and right edges of each disk. The reconstructions also contain distortions in the background in the form of vertical ‘bands’. Both the errors in the disks and the bands are a result of the errors in misestimating the Fourier components along the line $k_z = 0$ as well as those that correspond to waves incident at an angle larger than θ_c .

Figure 11(c) shows the reconstruction using Eq. (10) is shown for the case when T_s and T_l correspond to the solid (bone) layer being 1 mm thick. In this case, the minor distortions along the right and left edges of the disks are much more pronounced, resulting in what appear to be small objects near the disks. Likewise, the vertical banding is significantly more pronounced. One notes that these errors—associated with misestimating components in the k_z -direction—are more pronounced because of the larger errors associated with the thicker bone layer (see Figs. 8 and 9). In both Fig. 11(b) and 11(c), the horizontal and near-horizontal boundaries of the disks are estimated much better than the vertical boundaries. This is consistent with the fact that neglecting shear waves results in very little error in the Fourier components corresponding to propagating longitudinal waves in the solid layer (i.e., waves incident at an angle less than θ_c). One notes that previous studies in transcranial PAT^{14–17} did not possess these banding artifacts; however, the measurement geometry was not planar in those studies, which can result in different manifestations of the artifacts.

5 Summary and Discussion

In this work, a recently-introduced PAT image reconstruction algorithm, for use when the optical absorber is embedded in a layered medium that supports shear waves in some of the layers, was employed to determine the role shear waves play in PAT image formation. Using system parameters relevant to transcranial PAT, it was shown that, when shear waves are omitted from the imaging model, a smaller number of spatial frequency components of the object can be estimated compared to situations when shear waves are included. The spatial frequency components that are no longer accurately able to be estimated are components parallel to the layered medium and consistent with planewave components incident beyond the critical angle of the solid-fluid interface. These mis-estimated Fourier components result in distortions in the reconstructed

images. The strength of the distortions are directly related to the thickness of the solid (bone) layer.

The Fourier-based reconstruction method for inverting pressure data by disregarding shear waves in PAT imaging algorithms is mathematically equivalent to standard time-reversal (TR) and filtered backprojection (FBP) algorithms for PAT when the object of interest is embedded in a layered medium and acoustic detection is made on a continuous measurement surface. Since standard formulations of TR and FBP algorithms are insensitive to shear waves, images produced by these methods will exhibit the same systematic error as presented here. One notes that the geometry and type of transducers used to approximate a continuous measurement surface will also affect the systematic error introduced by not including shear waves.

The electrical and spatial impulse responses due to transduction and the finite size of each transducer, respectively, can be modeled as filters.^{20,28} In the Fourier representation of the photoacoustic field presented in this work, the effects from the transducers would be modeled by a multiplicative factor in the denominator of the right hand side of Eq. (5). The electrical impulse response often serves to diminish very low temporal frequency information, which corresponds to eliminating data from the center of Ewald’s sphere. Depending on the size and shape, the spatial pass-band of the transducer may diminish data from Ewald’s sphere that correspond to high spatial frequencies, that is, data for which the largest errors occur by not accounting for shear waves. Much wider pass-bands in both spatial and temporal frequencies occur when using planar, polymer-film ultrasound sensors²⁹ to acquire the photoacoustic signal.

For the reconstruction formula that compensates for shear waves, estimates of \mathcal{A} in the k_z -direction are non-uniformly sampled due to the relationship found in Eq. (6). To attain estimates of $A(\mathbf{r})$ from the non-uniformly sampled data, either interpolation of the data to a uniform grid in k_z followed by an FFT is required, or both steps can be performed at once using a non-uniform FFT (NUFFT).³⁰ In either case, the interpolation is performed along vertical lines in the Ewald sphere. One notes that the error maps shown in Figs. 7–10 exhibit errors that are non uniform in the k_z -direction.

There are a number of open problems that remain to be addressed in regards to accounting for shear wave physics in transcranial PAT. The manner in which neglecting shear waves affects image quality when different image reconstruction algorithms and non-planar imaging geometries are employed has not been investigated systematically. The non-uniform shape of the skull will certainly induce different types of

artifacts than the ‘bands’ presented in this work. The interplay between transducer placement/geometry and the errors described in this manuscript associated with neglecting shear waves is also an important topic of future investigation.

In some cases, the properties of the solid layer may not be determined accurately. One notes that mis-estimation of the acoustic absorption properties in the bone layer will affect both the phase (through using the wrong dispersion model) and the amplitude of the Fourier components of the object. Methods for estimating the acoustic absorption properties of bone that are sufficiently accurate to facilitate transcranial PAT applications remains an ongoing research topic.

When the shear wave properties are not known, it may be possible to develop an iterative reconstruction algorithm which uses the error maps found in Sec. 4 to create reconstructions using only the ‘minimal error’ components of the measured data. One notes that the regions of the Ewald sphere that possess minimal error are bounded by the critical angle of the solid-fluid interface for longitudinal waves when the solid layer is on the order of a millimeter or larger. That is, the region of estimable Fourier components depends only on the properties of the longitudinal waves in the medium. The development of such an algorithm remains as future work.

Appendix

In this Appendix, we derive the ATF for a three layered system in which the middle layer supports shear waves. The wavenumber in each layer is defined

$$k_m = \frac{\omega}{c_m(\omega)} + i\alpha_m\omega^s, \quad (11)$$

where $m = 0, 1, 2$, s labels the longitudinal modes in layers 0, 1 and 2 or the shear mode in layer 1. Neither dispersion or absorption is assumed in layers 0 and 2, so α_m is set to zero for those two layers. The Lamé coefficients, which describe the stiffness of the medium, are defined in the solid layer by

$$\lambda_1(\omega) = \rho \left[\frac{\omega^2}{k_1^2} - 2 \frac{\omega^2}{k_s^2} \right], \quad (12)$$

$$\mu_1(\omega) = \rho \frac{\omega^2}{k_s^2}, \quad (13)$$

and in the two fluid layers ($m = 0, 2$) by

$$\lambda_m = \rho_m c_m^2, \quad (14)$$

$$\mu_m = 0. \quad (15)$$

At the boundary between solid and fluid layers, the following boundary conditions apply to the acoustic field in terms of the particle displacement:

$$\hat{z} \cdot \mathbf{u}(\mathbf{r}, \omega)|_{z=z_n^-} = \hat{z} \cdot \mathbf{u}(\mathbf{r}, \omega)|_{z=z_n^+}, \quad (16)$$

$$\sigma_{zz}|_{z=z_n^-} = \sigma_{zz}|_{z=z_n^+}, \quad (17)$$

$$\sigma_{xz}|_{z=z_n^-} = 0, \quad (18)$$

$$\sigma_{yz}|_{z=z_n^-} = 0, \quad (19)$$

where z_n^- refers to the side of the boundary in the solid layer and it is assumed that the boundaries are all of the form $z = z_n$. The σ_{ij} denote stresses on the boundary, and take the form (in layer n)

$$\sigma_{zz} = \lambda_n \nabla \cdot \mathbf{u} + 2\mu_n \frac{\partial}{\partial z} u_z, \quad (20)$$

$$\sigma_{xiz} = \mu_n \left(\frac{\partial}{\partial x_i} u_z + \frac{\partial}{\partial z} u_{x_i} \right), \quad x_i = x, y. \quad (21)$$

The particle displacement is found from the pressure by

$$\rho\omega^2 \mathbf{u}(\mathbf{r}, \omega) = \nabla p(\mathbf{r}, \omega). \quad (22)$$

Application of the above boundary conditions on the planes z_1 and z_2 under the assumption of planewave insonification result in six independent equations relating the pressure fields in each layer. At the interface at $z = z_2$ the boundary equations reduce to

$$\begin{aligned} \lambda_2(\omega)k_2[1 + R(\mathbf{k}_{\parallel}, \omega)] &= f_1(\mathbf{k}_{\parallel}, \omega)[B(\mathbf{k}_{\parallel}, \omega) + C(\mathbf{k}_{\parallel}, \omega)] \\ &+ f_2(\mathbf{k}_{\parallel}, \omega)[D(\mathbf{k}_{\parallel}, \omega) \\ &+ F(\mathbf{k}_{\parallel}, \omega)], \end{aligned} \quad (23)$$

$$\begin{aligned} \frac{k_z^{(2)}}{k_2}[1 - R(\mathbf{k}_{\parallel}, \omega)] &= \frac{k_z^{(1)}}{k_1}[B(\mathbf{k}_{\parallel}, \omega) - C(\mathbf{k}_{\parallel}, \omega)] \\ &- \frac{k_{\parallel}}{k_s}[D(\mathbf{k}_{\parallel}, \omega) - F(\mathbf{k}_{\parallel}, \omega)], \end{aligned} \quad (24)$$

and

$$\begin{aligned} \frac{2k_z^{(2)}}{k_2}[B(\mathbf{k}_{\parallel}, \omega) - C(\mathbf{k}_{\parallel}, \omega)] \\ + f_3(\mathbf{k}_{\parallel}, \omega)[D(\mathbf{k}_{\parallel}, \omega) - F(\mathbf{k}_{\parallel}, \omega)] &= 0, \end{aligned} \quad (25)$$

where

$$f_1(\mathbf{k}_{\parallel}, \omega) = \lambda_1(\omega)k_1 + 2\mu_1(\omega) \frac{(k_z^{(1)})^2}{k_1}, \quad (26)$$

$$f_2(\mathbf{k}_{\parallel}, \omega) = -2\mu_1(\omega) \frac{k_z^{(s)}k_{\parallel}}{k_s}, \quad (27)$$

$$f_3(\mathbf{k}_{\parallel}, \omega) = \frac{2(k_z^{(s)})^2 - k_s^2}{k_{\parallel}k_s}. \quad (28)$$

The term R represents the pressure wave reflected back into layer 2 from the plane $z = z_2$, B and C represent the upward and downward moving longitudinal waves generated in layer 1, and D and F represent the upward and downward moving shear waves generated in layer 1 (see Fig. 12).

At the interface at $z = z_1$, the boundary conditions reduce to,

$$\begin{aligned} \lambda_0(\omega)k_0T(\mathbf{k}_{\parallel}, \omega) &= f_1(\mathbf{k}_{\parallel}, \omega)[B(\mathbf{k}_{\parallel}, \omega)e^{ik_z^{(1)}d_1} \\ &+ C(\mathbf{k}_{\parallel}, \omega)e^{-ik_z^{(1)}d_1}] \\ &+ f_2(\mathbf{k}_{\parallel}, \omega)[D(\mathbf{k}_{\parallel}, \omega)e^{ik_z^{(s)}d_1} \\ &+ F(\mathbf{k}_{\parallel}, \omega)e^{-ik_z^{(s)}d_1}], \end{aligned} \quad (29)$$

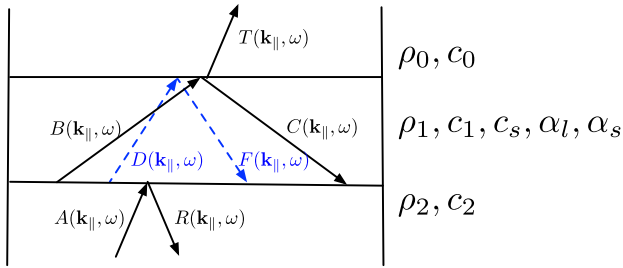


Fig. 12 A schematic of the planewave amplitudes in each layer for an incident pressure wave $A(\mathbf{k}_{\parallel}, \omega)$ with temporal frequency ω and transverse wavevector \mathbf{k}_{\parallel} . The dashed blue lines represent upward- and downward-traveling shear waves, and the solid black lines represent upward- and downward-traveling longitudinal waves. Note that $A(\mathbf{k}_{\parallel}, \omega) = 1$ for the purposes of this paper.

$$\frac{k_z^{(0)}}{k_0} T(\mathbf{k}_{\parallel}, \omega) = \frac{k_z^{(1)}}{k_1} [B(\mathbf{k}_{\parallel}, \omega) e^{ik_z^{(1)} d_1} - C(\mathbf{k}_{\parallel}, \omega) e^{-ik_z^{(1)} d_1}] - \frac{k_{\parallel}}{k_s} [D(\mathbf{k}_{\parallel}, \omega) e^{ik_z^{(s)} d_1} - F(\mathbf{k}_{\parallel}, \omega) e^{-ik_z^{(s)} d_1}], \quad (30)$$

and

$$\frac{2k_z^{(2)}}{k_2} [B(\mathbf{k}_{\parallel}, \omega) e^{ik_z^{(1)} d_1} - C(\mathbf{k}_{\parallel}, \omega) e^{-ik_z^{(1)} d_1}] \quad (31)$$

$$+ f_3(\mathbf{k}_{\parallel}, \omega) [D(\mathbf{k}_{\parallel}, \omega) e^{ik_z^{(s)} d_1} - F(\mathbf{k}_{\parallel}, \omega) e^{-ik_z^{(s)} d_1}] = 0. \quad (32)$$

The term T represents the pressure field transmitted into layer 0 from the plane $z = z_1$. This system of six linear equations are solved for each planewave component and temporal frequency to evaluate T in Eq. (5).

Acknowledgments

Robert W. Schoonover and Mark A. Anastasio acknowledge support in part by NIH awards EB010049 and EB009715. Lihong V. Wang acknowledge support by the NIH awards EB010049, CA134539, EB000712, CA136398, and EB008085. L.V.W. has a financial interest in Microphotoacoustics, Inc. and Endra, Inc., which, however, did not support this work.

References

1. L. V. Wang, "Prospects of photoacoustic tomography," *Med. Phys.* **35**(12), 5758–5767 (2008).
2. M. Xu and L. V. Wang, "Photoacoustic imaging in biomedicine," *Rev. Sci. Instrum.* **77**(4), 041101 (2006).
3. A. A. Oraevsky and A. A. Karabutov, "Optoacoustic tomography," in *Biomedical Photonics Handbook*, T. Vo-Dinh, Ed., CRC Press, Boca Raton, FL (2003).
4. L. Wang, ed., *Photoacoustic Imaging and Spectroscopy*, CRC Press, Boca Raton, FL (2009).
5. X. Wang et al., "Noninvasive laser-induced photoacoustic tomography for structural and functional *in vivo* imaging of the brain," *Nat. Biotechnol.* **21**(7), 803–806 (2003).
6. S. Yang et al., "Functional imaging of cerebrovascular activities in small animals using high-resolution photoacoustic tomography," *Med. Phys.* **34**(8), 3294–3301 (2007).
7. H. Brecht et al., "Whole-body three-dimensional optoacoustic tomography system for small animals," *J. Biomed. Opt.* **14**(6), 064007 (2009).
8. V. Ntziachristos and D. Razansky, "Molecular imaging by means of multispectral optoacoustic tomography (MSOT)," *Chem. Rev.* **110**(5), 2783–2794 (2010).
9. R. Kruger, D. Reinecke, and G. Kruger, "Thermoacoustic computed tomography- technical considerations," *Med. Phys.* **26**(9), 1832–1837 (1999).
10. M. Haltmeier et al., "Thermoacoustic computed tomography with large planar receivers," *Inverse Probl.* **20**(5), 1663–1673 (2004).
11. P. Ephrat et al., "Three-dimensional photoacoustic imaging by sparse-array detection and iterative image reconstruction," *J. Biomed. Opt.* **13**(5), 054052 (2008).
12. B. T. Cox et al., "Two-dimensional quantitative photoacoustic image reconstruction of absorption distributions in scattering media by use of a simple iterative method," *Appl. Opt.* **45**(8), 1866–1875 (2006).
13. K. Wang et al., "An imaging model incorporating ultrasonic transducer properties for three-dimensional optoacoustic tomography," *IEEE T. Med. Imaging* **30**(2), 203–214 (2011).
14. Y. Xu and L. Wang, "Rhesus monkey brain imaging through intact skull with thermoacoustic tomography," *IEEE T. Ultrason. Ferr.* **53**(3), 542–548 (2006).
15. X. Jin, C. Li, and L. V. Wang, "Effects of acoustic heterogeneities on transcranial brain imaging with microwave-induced thermoacoustic tomography," *Med. Phys.* **35**(7), 3205–3214 (2008).
16. X. Yang and L. V. Wang, "Monkey brain cortex imaging by photoacoustic tomography," *J. Biomed. Opt.* **13**(4), 044009 (2008).
17. L. Nie, Z. Guo, and L. Wang, "Photoacoustic tomography of monkey brain using virtual point ultrasonic transducers," *J. Biomed. Opt.* **16**(7), 076005 (2011).
18. B. E. Treeby, E. Z. Zhang, and B. T. Cox, "Photoacoustic tomography in absorbing acoustic media using time reversal," *Inverse Probl.* **26**(11), 115003 (2010).
19. R. W. Schoonover and M. A. Anastasio, "Compensation of shear waves in photoacoustic tomography with layered acoustic media," *J. Opt. Soc. Am. A* **28**(10), 2091–2099 (2011).
20. Y. Xu, D. Feng, and L. V. Wang, "Exact frequency-domain reconstruction for thermoacoustic tomography: I. planar geometry," *IEEE T. Med. Imaging* **21**(7), 823–828 (2002).
21. R. W. Schoonover and M. A. Anastasio, "Image reconstruction in photoacoustic tomography involving layered acoustic media," *J. Opt. Soc. Am. A* **28**(6), 1114–1120 (2011).
22. P. Droin, G. Berger, and P. Laugier, "Velocity dispersion of acoustic waves in cancellous bone," *IEEE T. Ultrason. Ferr.* **45**(3), 581–592 (1998).
23. K. Waters et al., "On the applicability of Kramers–Kronig relations for ultrasonic attenuation obeying a frequency power law," *J. Acoust. Soc. Am.* **108**(2), 556–563 (2000).
24. P. White, G. Clement, and K. Hynynen, "Local frequency dependence in transcranial ultrasound transmission," *Phys. Med. Biol.* **51**(9), 2293–2305 (2006).
25. K. Waters and B. Hoffmeister, "Kramers-Kronig analysis of attenuation and dispersion in trabecular bone," *J. Acoust. Soc. Am.* **118**(6), 3912–3920 (2005).
26. S. Chaffai et al., "In vitro measurement of the frequency-dependent attenuation in cancellous bone between 0.2 and 2 mhz," *J. Acoust. Soc. Am.* **108**(3), 1281–1289 (2000).
27. S. Pichardo, V. Sin, and K. Hynynen, "Multi-frequency characterization of the speed of sound and attenuation coefficient for longitudinal transmission of freshly excised human skulls," *Phys. Med. Biol.* **56**(1), 219–250 (2011).
28. K. Wang et al., "An imaging model incorporating ultrasonic transducer properties for three-dimensional optoacoustic tomography," *IEEE T. Med. Imaging* **30**(2), 203–214 (2011).
29. E. Zhang, J. Laufer, and P. Beard, "Backward-mode multiwavelength photoacoustic scanner using a planar fabry-perot polymer film ultrasound sensor for high-resolution three-dimensional imaging of biological tissues," *Appl. Opt.* **47**(4), 561–577 (2008).
30. R. Schulze et al., "On the use of frequency-domain reconstruction algorithms for photoacoustic imaging," *J. Biomed. Opt.* **16**(8), 086002 (2011).